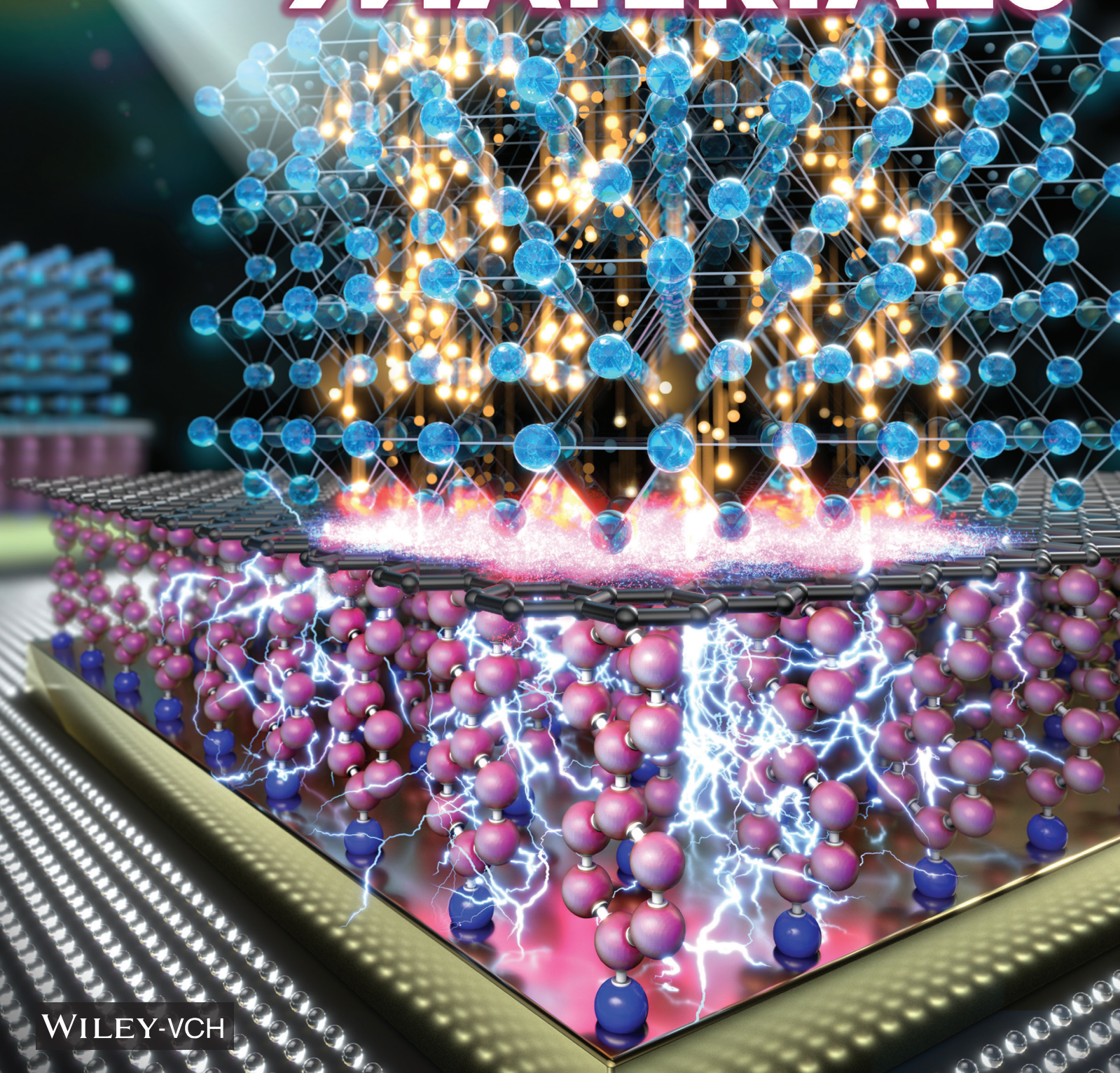


Vol. 10 • No. 11 • June 3 • 2022

[www.advopticalmat.de](http://www.advopticalmat.de)

# ADVANCED OPTICAL MATERIALS



WILEY-VCH

# Photo-Responsive Molecular Junctions Activated by Perovskite/Graphene Heterostructure Electrode

Changjun Lee, Junwoo Kim, Jonghoon Lee, Woocheol Lee, Minwoo Song, Kyeong-Yoon Baek, Jiwon Shin, Jongwoo Nam, Jeongjae Lee, Keehoon Kang,\* and Takhee Lee\*

Photoresponsivity is a fundamental process that constitutes optoelectronic devices. In molecular junction devices, one of the most adopted strategies is to employ photoactive molecules that can undergo conformational change upon light illumination as the conduction channel. However, such devices suffer from their relatively low photoresponsivity, long switching time, and unidirectional switching. In this study, the authors employed organohalide perovskite (OHP)/graphene heterojunction as a photoactive electrode that acted as a source of photo-generated carriers collected as photocurrent in self-assembled monolayer (SAM)-based molecular junctions. This hybrid device architecture of perovskite/graphene/SAM allows the molecular junctions to attain a high photoresponsivity with molecules that have intrinsically little photoresponse. The authors elucidate the role of the molecular SAM in enhancing the photoresponsivity by systematically examining the transport and charge transfer processes at the graphene/SAM interface via molecules with different intrinsic dipole moments. This, corroborated with a theoretical analysis, reveals the origin of the observed photoresponsivity as light-induced coupling between the SAM and the OHP/graphene electrode within the orbital-mediated resonant tunnelling transport regime. These findings advance the understanding of photo-induced charge transport in molecular junctions with heterointerfaces, providing a road-map for designing high-performance molecular optoelectronic devices based on hybrid device architecture.

## 1. Introduction

In the field of molecular electronics, various studies have been conducted to achieve the ultimate miniaturization of electronic circuits.<sup>[1–8]</sup> Many significant developments have been made to utilize single or bundles of molecules as electronic components such as molecular wires, rectifiers, transistors, memories, switches, and thermoelectric devices.<sup>[9–18]</sup> Regardless of the types of devices, it is crucial to understand and control the charge transport characteristics through molecular junctions. Charge transport phenomena in molecular junctions are influenced by not only the electrical characteristics of molecules but also the interactions that occur at the interfaces between molecules and electrodes.<sup>[19–23]</sup> Therefore, taking into account the electrical properties of the electrodes and their interaction with molecules, the choice of electrode material is important in determining the overall charge transport properties of the molecular junctions.

Since the self-assembled monolayers (SAMs) of molecules are typically chemisorbed onto the bottom electrodes, the


choices of the bottom electrodes are limited; for example, the end groups of molecules such as thiol group form covalent bonding on the electrodes such as Au and Ag.<sup>[24]</sup> For this reason, changing top electrodes has been used as a preferred way to tailor the charge transfer through molecular junctions. Several materials and methods have been suggested as top electrodes of molecular junctions, such as liquid metals, evaporated or transferred metals, conducting polymers, graphene film, etc.<sup>[25–27]</sup> The development of these junctions has contributed to producing stable molecular junctions with high yield and enabled charge transport modulation using engineering treatments for the top electrodes.<sup>[28,29]</sup> However, once a molecular junction is manufactured, these conductive materials of electrodes have a fixed work function regardless of using pristine or engineered materials, thus limiting the further modulation of charge transport properties of the molecular junctions.

In this context, illuminating light can be an attractive tool to make in-situ controllable molecular junctions due to its

C. Lee, J. Kim, J. Lee, W. Lee, M. Song, K.-Y. Baek, J. Shin, J. Nam, T. Lee  
Department of Physics and Astronomy  
Institute of Applied Physics  
Seoul National University  
Seoul 08826, Korea  
E-mail: tlee@snu.ac.kr

J. Lee  
School of Earth and Environmental Sciences  
Seoul National University  
Seoul 08826, Korea

K. Kang  
Department of Materials Science and Engineering  
Research Institute of Advanced Materials  
Institute of Applied Physics  
Seoul National University  
Seoul 08826, Korea  
E-mail: keeho.kang@snu.ac.kr

 The ORCID identification number(s) for the author(s) of this article can be found under <https://doi.org/10.1002/adom.202200049>.

DOI: 10.1002/adom.202200049

continuous characteristics, good addressability, and compatibility with solid-state device structures. Conventionally, optical control of the charge transport in a molecular junction was implemented by employing intrinsically photo-active molecules whose molecular conformation changes upon photo-excitation.<sup>[30–32]</sup> However, SAM-based molecular junctions with photo-switching molecules suffer from either long switching times or irreversible switching properties.<sup>[33–35]</sup> Therefore, rather than relying on the intrinsically photo-active molecules, functionalizing other device components (e.g., electrodes) can be a suitable engineering option to explore the photo-modulated conduction properties in molecular junctions.

In order to effectively achieve photo-modulated charge transport characteristics of molecular junctions via engineering the electrodes, a well-designed electrode with the following features are required: high light absorption coefficient, efficient carrier photo-generation, and effective charge transfer to the active SAM. In this regard, organohalide perovskite (OHP) is an excellent candidate as a photo-active layer that can be integrated to the top electrode of the molecular junctions. OHPs have recently attracted significant attention due to their outstanding photophysical properties, such as their high absorption coefficient, low exciton binding energy, and long carrier lifetime.<sup>[36–38]</sup> Owing to their high quantum efficiency, numerous carriers can be generated when exposed to light, which can enhance the current of the molecular junctions. However, the OHP itself is not a suitable electrode material due to its poor conductivity.<sup>[39,40]</sup> Thus, it is better to use OHP as a light-absorbing layer and use another conductive material that is capable of effectively accommodating the photo-generated charges in the OHP. For this purpose, monolayer graphene, which has the advantage of the atomically thin feature, allows photo-generated carriers to transit easily from the photo-active OHP layer to SAMs. In addition, the well-known electronic structure of graphene helps to analytically investigate the interfacial phenomena that occur when in contact with SAMs and OHPs.<sup>[41]</sup>

In this study, we implemented photo-modulated molecular junctions by employing an OHP/graphene heterostructure on SAMs. Through a single-source flash evaporation, we deposited the patterned and uniform methylammonium lead iodide (denoted as MAPbI<sub>3</sub>) OHP film as a photo-active layer on the graphene. The electronic band properties of MAPbI<sub>3</sub>/graphene interface were then investigated, and their response to light illumination was observed. To distinguish the role of SAM in the charge modulation, we fabricated two-terminal control devices without SAMs and quantitatively examined the electrical properties under dark and light illumination conditions. Then, we fabricated molecular junction devices with MAPbI<sub>3</sub>/graphene/SAMs/Au structure to demonstrate the dependence of their charge transport modulation characteristics on light intensity. For further improvement in photocurrent to dark current ratio (PDR), we explored several molecules with different electric dipole moments to vary the MAPbI<sub>3</sub>/graphene/SAM interface effect. Theoretical analysis based on Landauer formalism was performed to corroborate our experimental results and elucidate the role of SAMs and their interaction with MAPbI<sub>3</sub>/graphene heterostructure.

## 2. Results and Discussion

Figure 1a shows the schematic image of the fabricated OHP/graphene/SAM/Au structure. Patterned holes and photoresist walls were made by conventional photolithography. Chemical vapor deposition (CVD)-grown monolayer graphene was transferred via wet transfer method.<sup>[42]</sup> The perovskite film was then deposited through the single-source evaporation method, as we previously reported.<sup>[43,44]</sup> The detailed fabrication process is described in the Experimental Section and depicted in Figure S1, Supporting Information. Figure 1b shows images sequentially magnified from a whole substrate piece to a molecular junction from left to right in order: entire and enlarged optical microscope images of fabricated molecular junction devices on substrates, an atomic force microscope (AFM) image of a hole with a radius of 2 μm, and a cross-sectional transmission electron microscope (TEM) image of a molecular junction. The molecules used in this study are listed in Figure 1c. To achieve efficient charge transport modulation via electrode engineering, we selected several conjugated molecules rather than saturated molecules (e.g., alkanethiols) due to their relatively better conductivity, which originated from the small gap between the highest occupied molecular orbital (HOMO) and the lowest unoccupied molecular orbital (LUMO).<sup>[45–47]</sup> According to the direction of the intrinsic electric dipole moment, we used biphenyl-4-thiol (denoted as BPT), 1,4-benzenedithiol (BDT), and pentafluorobenzenethiol (PFBT) in this study. BPT has an electric dipole oriented upwardly away from the thiol (–SH) group, whereas PFBT has an electric dipole in the opposite direction (i.e., toward the thiol group). BDT is considered to have the weakest electrical dipole moment due to its symmetric structure. The monolayer graphene was characterized by measuring the Raman spectroscopy through the G and 2D peaks at energy shifts of 1580 and 2680 cm<sup>–1</sup>, respectively (Figure 1d). As shown in Figure 1e, OHP has the crystal structure of ABX<sub>3</sub>, where A is a small cation (e.g., methylammonium, denoted as MA), B is a metal ion (e.g., Pb<sup>2+</sup> or Sn<sup>2+</sup>), and X is a halide (e.g., I<sup>–</sup>, Br<sup>–</sup>, or Cl<sup>–</sup>). In several studies, OHP films were deposited on graphene through the spin-coating method.<sup>[48,49]</sup> However, it has been challenging to form a uniform, full-coverage OHP film using the typical solvents for OHP solutions such as dimethylformamide, dimethyl sulfoxide, and gamma-butyrolactone due to their polar characteristics.<sup>[50]</sup> Therefore, we used the single-source evaporation method to deposit a high-quality film of OHP with high uniformity and without pinholes, regardless of the surface energy on the substrate material.<sup>[43,44]</sup> First, MAPbI<sub>3</sub> powder, which can be used as the flash-evaporation source, was synthesized with high purity and characterized by powder X-ray diffraction (XRD) spectra (Figure S2, Supporting Information). Field-emission scanning electron microscope (FE-SEM) images, shown in Figure 1f, confirmed that a pinhole-free and uniform MAPbI<sub>3</sub> film with a film thickness of ≈200 nm was formed by the flash evaporation (bottom image of Figure 1f). The quality of the deposited MAPbI<sub>3</sub> film was characterized by XRD (Figure 1g), absorbance, and AFM images (Figure S3, Supporting Information), indicating that MAPbI<sub>3</sub> film was formed with good quality. In Figure 1g, large diffraction peaks of MAPbI<sub>3</sub> film were located at 14.08° and 28.44°, corresponding to the crystallographic

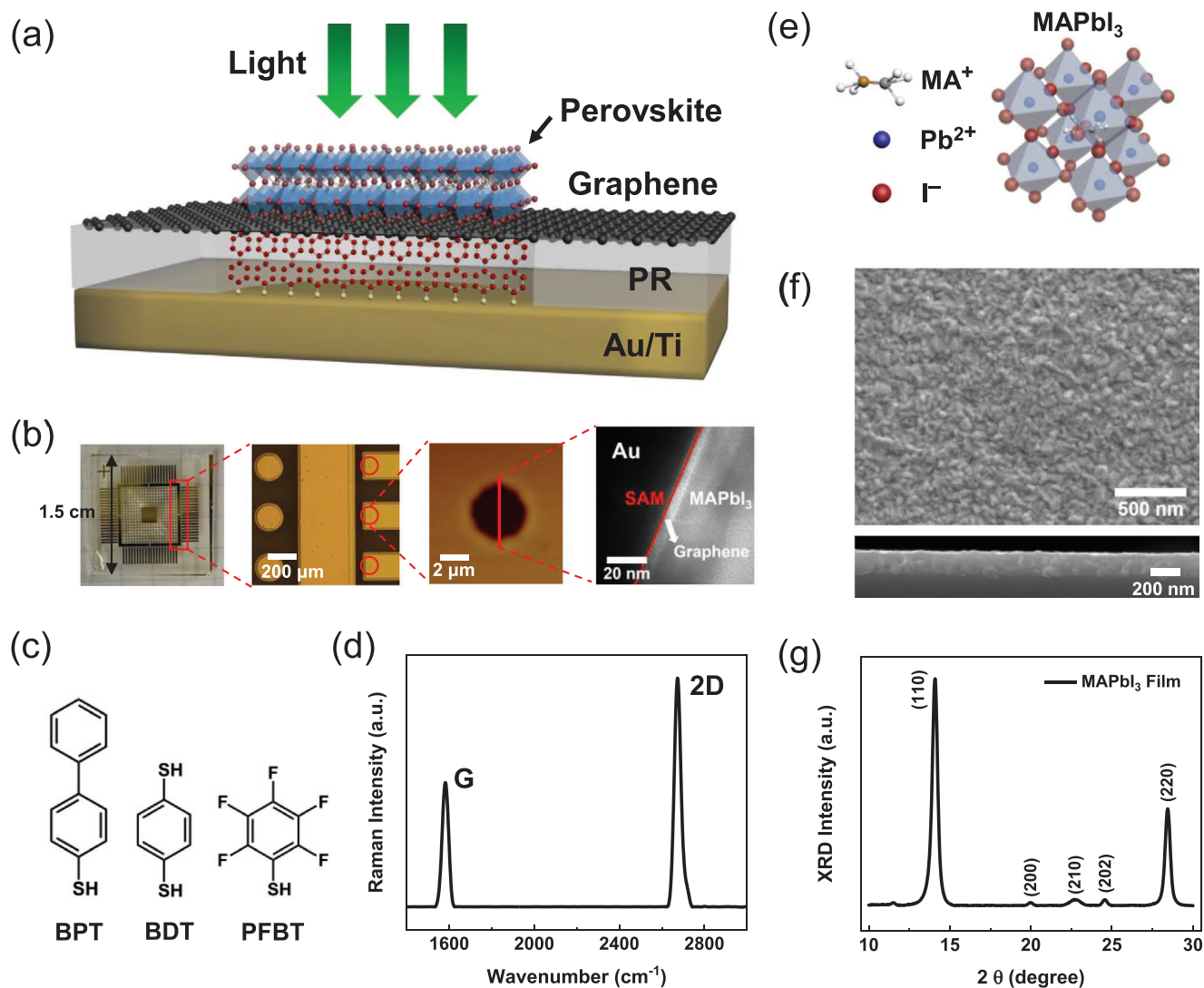


**Figure 1.** a) Schematic illustration of a fabricated molecular junction. b) Optical, AFM, and TEM images of the fabricated molecular devices. From left to right in order, entire and enlarged optical images of fabricated molecular junctions on substrates, AFM image of a hole, and cross-sectional TEM image of a molecular junction. c) Molecules used in this study. From left to right in order, biphenyl-4-thiol (BPT), 1,4-benzenedithiol (BDT), and pentafluorobenzenethiol (PFBT). d) Raman spectrum of the monolayer graphene. e) Schematic illustration of MAPbI<sub>3</sub>. f) Topological and cross-sectional FE-SEM images of the deposited MAPbI<sub>3</sub> film. g) XRD pattern of the deposited MAPbI<sub>3</sub> film.

planes (110) and (220), respectively. Minor peaks of the (200), (211), and (202) planes were also detected at  $2\theta$  values of  $19.98^\circ$ ,  $22.76^\circ$ , and  $24.58^\circ$ , respectively. From the absorbance spectra of the MAPbI<sub>3</sub>/graphene, the absorption edge was measured at 772 nm (optical bandgap  $\approx 1.6$  eV), representing that MAPbI<sub>3</sub> on graphene absorbs over the entire visible-light range (Figure S3, Supporting Information).<sup>[51]</sup> The roughness of the deposited MAPbI<sub>3</sub> film was found to be  $\approx 3.3$  nm through the AFM measurement (Figure S3, Supporting Information).

Before investigating the molecular junctions, we examined, as a control group, the electrical properties of the MAPbI<sub>3</sub>/graphene heterostructure in the absence of molecules. We used ultraviolet photoelectron spectroscopy (UPS) to verify the known work functions of monolayer graphene ( $\approx 4.4$  eV) and MAPbI<sub>3</sub> ( $\approx 3.9$  eV) (Figure 2a).<sup>[52,53]</sup> As depicted in Figure 2b, contact between MAPbI<sub>3</sub> and graphene initiates an internal

electric field at the MAPbI<sub>3</sub>/graphene interface due to the work function difference. Since the work function of the graphene is deeper than that of MAPbI<sub>3</sub>, the energy band is bent down toward the MAPbI<sub>3</sub> direction. Under light illumination, electron-hole pairs are generated and form excitons in the MAPbI<sub>3</sub> film. Then, the charge carriers (electrons and holes) are separated from the photo-generated excitons and injected into graphene with the aid of the internal field at the MAPbI<sub>3</sub>/graphene interface. This charge transfer phenomenon between the MAPbI<sub>3</sub> and graphene can be understood by observing the photoluminescence (PL) quenching phenomenon (Figure 2c). The PL peak positions of both MAPbI<sub>3</sub> film and MAPbI<sub>3</sub>/graphene heterostructure are located  $\approx 770$  nm, which corresponds to the band-to-band transition peak of  $\approx 1.6$  eV, similar to the previously reported values.<sup>[51]</sup> Without the PL peak shift, the maximal PL intensity of the MAPbI<sub>3</sub>/graphene was quenched

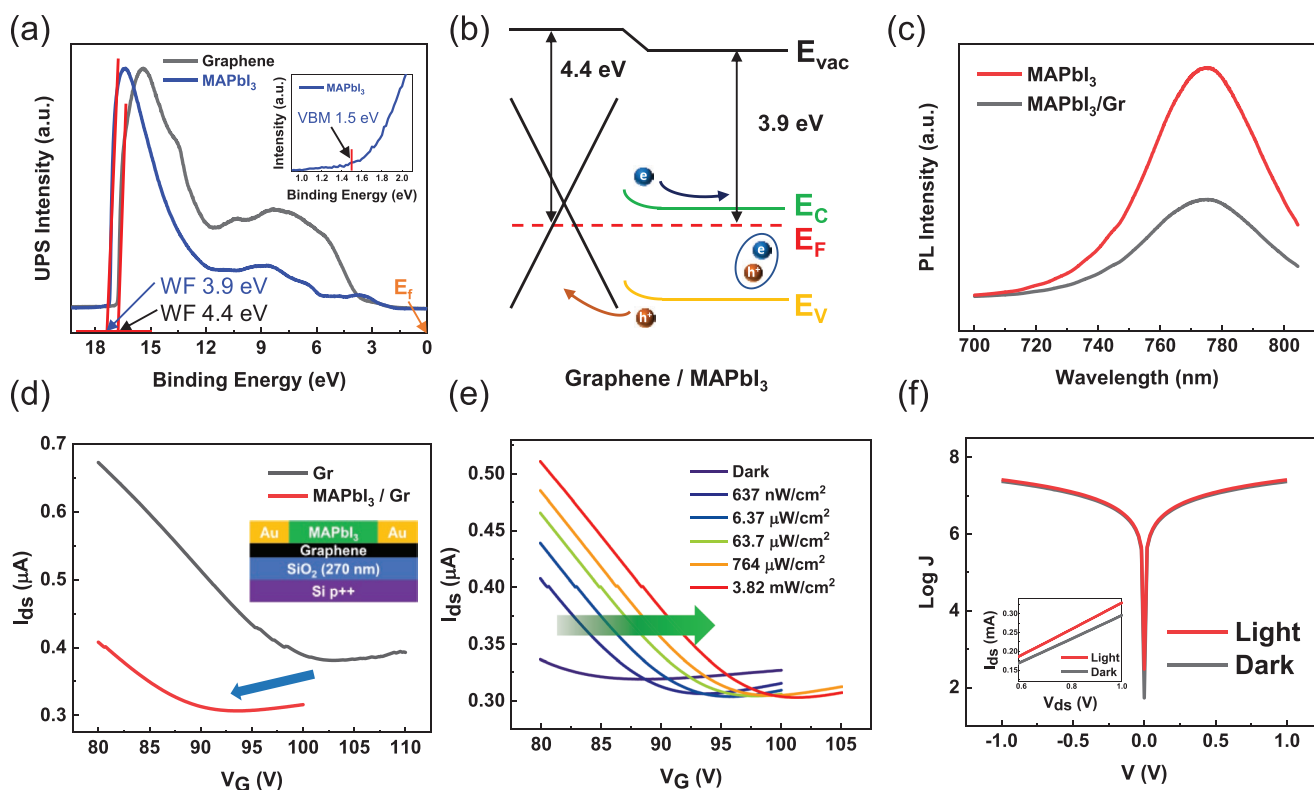


**Figure 2.** a) UPS spectra of the MAPbI<sub>3</sub> film using the single-source flash evaporation method and the monolayer graphene. b) Energy band diagram when the graphene and MAPbI<sub>3</sub> form a contact. c) PL spectra of the pristine MAPbI<sub>3</sub> film and MAPbI<sub>3</sub>/graphene heterostructure upon 532 nm excitation. d) I<sub>ds</sub>-V<sub>gs</sub> characteristics of a pristine GFET (denoted as Gr, black curve) and MAPbI<sub>3</sub>/graphene hybrid FET (denoted as MAPbI<sub>3</sub>/Gr, red curve). The inset shows the schematic image of a MAPbI<sub>3</sub>/Gr FET device. e) I<sub>ds</sub>-V<sub>gs</sub> curves of a MAPbI<sub>3</sub>/Gr FET showing a gradual p-doping effect as the light intensity increases. f) Electrical characteristics of a control device (MAPbI<sub>3</sub>/graphene/Au without SAM) under the light intensity of 3.82 mW cm<sup>-2</sup>. The left inset shows the I-V curve on linear scale and the right inset presents the schematic image of the fabricated control device.

by 55% compared to that of pristine MAPbI<sub>3</sub> film. This PL quenching phenomenon represents the effective charge transfer between the MAPbI<sub>3</sub> and graphene, resulting from the internal field at the interface and  $\pi$ - $\pi$  interaction between sp<sup>2</sup> hybridized graphene and MAPbI<sub>3</sub>.<sup>[48,54]</sup>

To directly verify the charge transfer from perovskite to graphene, we fabricated a graphene field-effect transistor (GFET) covered with the MAPbI<sub>3</sub> film as a light harvester and estimated how many photo-generated carriers were transferred and contributed to the photocurrent. As mentioned above, the electron transfer from MAPbI<sub>3</sub> to graphene due to the work function mismatch causes initial n-doping of the monolayer graphene (Figure 2d). When the light is illuminated, a photo-generated hole injection at the MAPbI<sub>3</sub>/graphene interface promotes the gradual p-doping of graphene (Figure 2e). The increase in the number of charge carriers in graphene with increasing light intensity can be calculated from the Dirac voltage values obtained experimentally, according to the following relations:<sup>[55,56]</sup>

$$V_{\text{gs}} - V_{\text{Dirac}} = \frac{E_f}{e} + \frac{e\Delta n}{C_{\text{ox}}} \quad (1)$$

$$\Delta n = \Delta(n_e - p_h) = \frac{2}{\pi} \left( \frac{k_B T}{\hbar v_f} \right)^2 \{ F_1(+\xi) - F_1(-\xi) \} \quad (2)$$

where  $e$  is the elementary charge,  $C_{\text{ox}}$  is the gate oxide capacitance per unit area,  $n_e$  and  $p_h$  are electron and hole densities, respectively,  $k_B$  is the Boltzmann constant,  $T$  is the temperature,  $\hbar$  is the reduced Planck constant,  $v_f$  is the Fermi velocity of graphene ( $\approx 10^6$  m s<sup>-1</sup>),  $F_1(\eta)$  is Fermi-Dirac integral  $F_j(\eta)$  with  $j = 1$ ,  $\xi = \frac{\Delta E}{k_B T}$ , and  $\Delta E$  is the energy difference between the Dirac point and the Fermi level of graphene. The detailed calculation procedure is described in Section S4, Supporting Information. Briefly, Equations (1) and (2) can be combined to extract the value of  $\Delta n = 11.5 \times 10^{11}$  cm<sup>-2</sup> under a light intensity of 3.82 mW cm<sup>-2</sup>. Given the intrinsic carrier concentration of graphene ( $\approx 9 \times 10^{12}$  cm<sup>-2</sup>),<sup>[57]</sup> the number of carriers in the monolayer graphene channel increased by  $\approx 13\%$  with respect to the intrinsic carrier concentration under a light intensity of 3.82 mW cm<sup>-2</sup>. In this manner, we measured the current-voltage (I-V) characteristics of a two-terminal control device (MAPbI<sub>3</sub>/graphene/Au without SAM) under dark and illuminated conditions. Even with a high-intensity illumination (3.82 mW cm<sup>-2</sup>) of 532 nm laser, the current enhancement due to the photocurrent generation was rather modest, exhibiting an increase of  $\approx 15\%$  with respect to the dark current (see Figure 2f). The consistency of this result with the  $\approx 13\%$  increase of carrier concentration derived from graphene field-effect transistor (GFET) measurement under the same light intensity supports our argument.

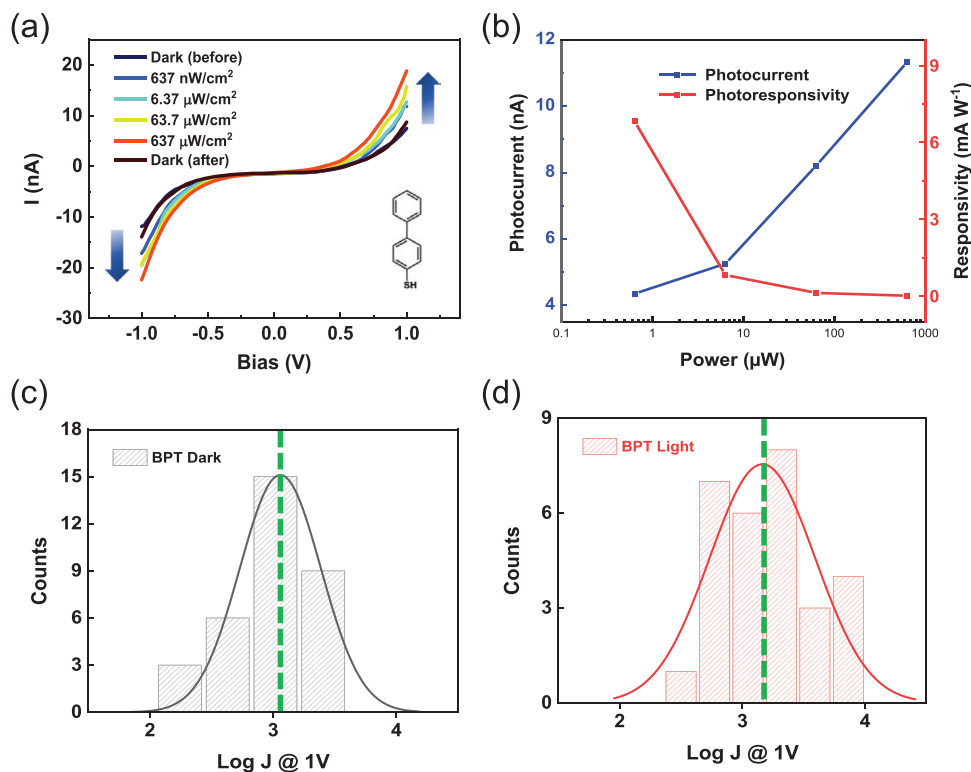


**Figure 3.** a)  $I$ - $V$  characteristics of the representative BPT-based molecular junction according to the light intensity. b) Photocurrent (= current when illuminated – current at dark condition) and photo responsivity data plot of Au/BPT/Graphene/MAPbI<sub>3</sub> junction. c,d) Statistical data with Gaussian fitting of logarithmic current densities of all BPT molecular junctions under the (c) dark and (d) light conditions. The mean logarithmic current densities at 1 V were represented as green dashed lines.

Figure 3 shows the electrical characteristics of MAPbI<sub>3</sub>/graphene/SAM/Au molecular junctions. We used BPT molecules for the SAM, which is one of the suitable molecules for our device structure due to the conductive nature originated from delocalized  $\pi$ -electrons.<sup>[58]</sup> As shown in Figure 3a, reversible and light intensity-dependent photocurrent modulation was observed for BPT molecular junctions. Specifically, the current increased  $\approx 250\%$  at 1 V under the highest light intensity (637  $\mu\text{W cm}^{-2}$ ) compared to the dark condition. Figure 3b,c shows the statistical analysis for the BPT molecular junctions. We plotted the histograms of the logarithmic current density (Log J) at 1 V of all working BPT molecular junctions and then performed Gaussian fittings on the histograms. Extracted average logarithmic current densities were found to be  $\approx 3.04$  ( $\approx 1.10 \times 10^3 \text{ A cm}^{-2}$  at 1 V) for the dark condition (Gaussian standard deviation  $\sigma$  of  $\approx 0.33$ ) and  $\approx 3.20$  ( $\approx 1.59 \times 10^3 \text{ A cm}^{-2}$  at 1 V) under the light illumination ( $\sigma$  of  $\approx 0.43$ ), corresponding to  $\approx 145\%$  photo-induced current enhancement. Note that PDR of BPT molecular junctions outperforms that of the control device without SAM ( $\approx 15\%$ ) by an order of magnitude. Such a significant difference between the systems with and without molecules implies that SAM plays an essential role in the photo-induced current enhancement, as discussed later.

However, this current enhancement of BPT molecular junctions is somewhat smaller than the previous results using photo-stimulated molecules such as diarylethene or azobenzene which have shown increases of about an order of magnitude.<sup>[30,33–35]</sup> In such context, for further improvement in

current enhancement at molecular junctions, we chose to vary the molecular dipole moment. Effect of dipoles on the transport characteristics had often considered to be elusive, due to depolarizations by disorders or interactions that occur among the molecules in SAM layer. However, depolarization effect did not appear to be dominant in our study in which the transport properties showed a clear dipole dependence probably due to a low packing density of phenyl-based molecule SAMs.<sup>[59,60]</sup> Moreover, a series of recent studies<sup>[61,62]</sup> have reported a critical role of dipoles in the charge transport behaviors in large area molecular junctions, which supports that the depolarization effect can be neglected in these junctions. BPT has an intrinsic dipole moment, oriented from the thiol group ( $\delta^-$ ) to the molecular backbone ( $\delta^+$ ). Since the injected holes from MAPbI<sub>3</sub> are major carriers of the photocurrent, the  $\delta^+$  partial charge at the side of BPT SAM hinders the charge transport of injected holes (Figure 4a). Hence, adjusting the direction of molecular dipole moments to facilitate hole injection would be expected to boost photo-induced current enhancement. For this purpose, we used BDT and PFBT molecules in addition to BPT. BDT has no intrinsic dipole due to its symmetric structure, and PFBT has a dipole moment in the direction opposite that of BPT, that is, oriented from the molecular backbone ( $\delta^-$ ) to the thiol group ( $\delta^+$ ).<sup>[63]</sup> The dipole moment of each molecule, as obtained through density functional theory (DFT) calculation, was  $\approx 1.01 \text{ D}$  for BPT,  $0.00 \text{ D}$  for BDT, and  $1.55 \text{ D}$  for PFBT (see Table S2, Supporting Information). The interruption of hole injection by dipole-induced field can be eliminated in the case of BDT, and

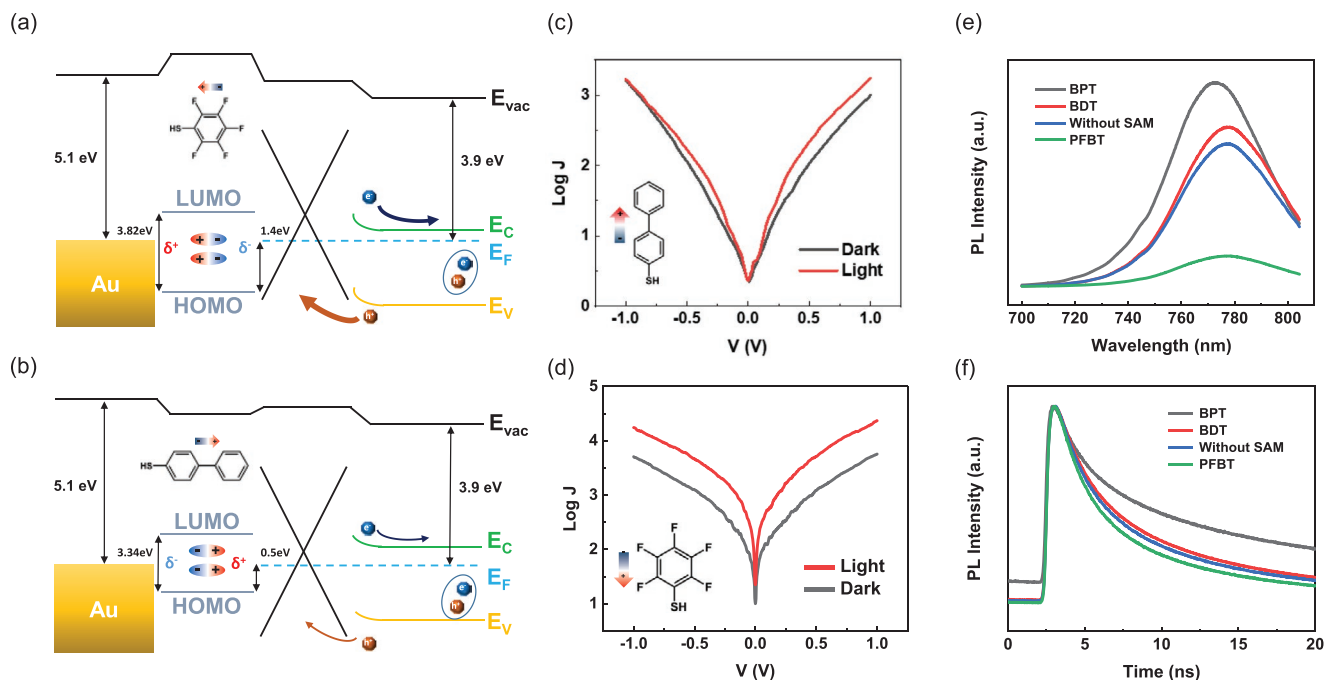


**Figure 4.** Photo-induced current enhancement by dipole-induced field variation. a,b) Schematic mechanism of photo-induced current enhancement by varying dipole moments. Band diagrams of a) BPT-based and b) PFBT-based molecular junction. c,d) Logarithmic average current densities according to the voltage for c) BDT and d) PFBT molecular junctions. Red and black lines represent the photocurrent and dark current, respectively. e) PL quenching characteristics according to the dipole direction. f) TRPL spectra of perovskite/graphene/SAM structure according to the dipole moment variation.

the  $\delta^-$  partial charge of PFBT SAM can provoke the injection of photo-generated holes from the MAPbI<sub>3</sub> film to molecular junctions (Figure 4b). Figures 4c and 4d show the average logarithmic current densities of BDT and PFBT molecular junctions, respectively. On average, PDR of 220% and 450% were obtained for BDT (Figure 4c) and PFBT (Figure 4d) molecular junctions, respectively. Especially, a  $\approx 1000\%$  current increase was observed for the best-performing PFBT molecular device. We used PL quenching and time-resolved photoluminescence (TRPL) spectra to corroborate this molecular dipole direction effect on performance behavior. Figure 4e shows the PL spectra of MAPbI<sub>3</sub>/graphene/SAM/Au junctions for all molecules used in this study. The PL intensity decreased the most in the PFBT case and the least in the BPT case. The stronger the  $\delta^-$  partial charges on the graphene side of the molecular dipole, the greater the PL intensity reduction due to the improved hole injection. In Figure 4e,f, “Without SAM” refers to the MAPbI<sub>3</sub>/graphene/Au junction lacking SAM. Figure 4f shows the TRPL spectra of MAPbI<sub>3</sub>/graphene/SAM/Au junctions. Average carrier lifetimes, extracted via conventional biexponential fitting to TRPL curves, were as follows:  $\approx 5.9$  ns for BPT, 3.0 ns for BDT, 2.6 ns for “Without SAM”, and 1.8 ns for PFBT. In agreement with the PL quenching and electrical data, the carrier lifetime decreased sequentially from BPT to PFBT as the strength of the dipole-assisted hole injection effect increased, again suggesting enhanced charge extraction from BPT to PFBT.

To elucidate the role of SAM on the photoinduced current enhancement of molecular junctions, we applied Landauer formalism to the obtained electrical data. In the case of conventional molecules with a large HOMO–lowest unoccupied molecular

orbital (LUMO) gap (e.g., alkanethiols), where the frontier orbital level is sufficiently far from the Fermi level, non-resonant direct tunneling governs the charge transport, which is usually described by the simplified Simmons model.<sup>[64]</sup> Indeed, the transport in our octanedithiol devices can well be described by Simmons’ model and they exhibited the photoinduced current enhancement of  $\approx 11\%$  (see Figure S9 and Section S10, Supporting Information, for more details). However, this simple direct tunneling model is unsuitable for justifying a significantly large photo-induced current enhancement by several hundred percent in a  $\pi$ -conjugated molecular junction devices. Since the HOMO level of the phenyl-ring-based molecules used in our study is comparatively close to the Fermi level, the resonant tunneling model is more relevant and useful than the Simmons model.<sup>[65]</sup> Assuming that electrons are transported coherently, we can describe the resonant tunneling current via Equation (3), which is used to fit the average  $I$ – $V$  curves of BPT (Figure 5a) and PFBT molecular junctions (Figure 5b).<sup>[47,66]</sup>

$$I(V) = \int_{-\infty}^{\infty} T(E, V) [f_B(E) - f_T(E + eV)] dE \quad (3)$$

where  $E$  is the energy of the charge carrier,  $f_X(E)$  is the Fermi-Dirac distribution of each electrode given by Equation (4), and  $T(E, V)$  is the transmission function given by Equation (5).

$$f_X(E) = \left(1 + \exp\left(\frac{E - \mu_X}{k_B T}\right)\right)^{-1} \quad (4)$$

where  $\mu_X$  is the Fermi level of electrodes and  $X = \text{top or bottom}$ .

$$T(E, V) = \frac{4\Gamma_T\Gamma_B}{\left((\Gamma_T + \Gamma_B)^2 + (E - E_0 + \alpha eV)^2\right)} \quad (5)$$

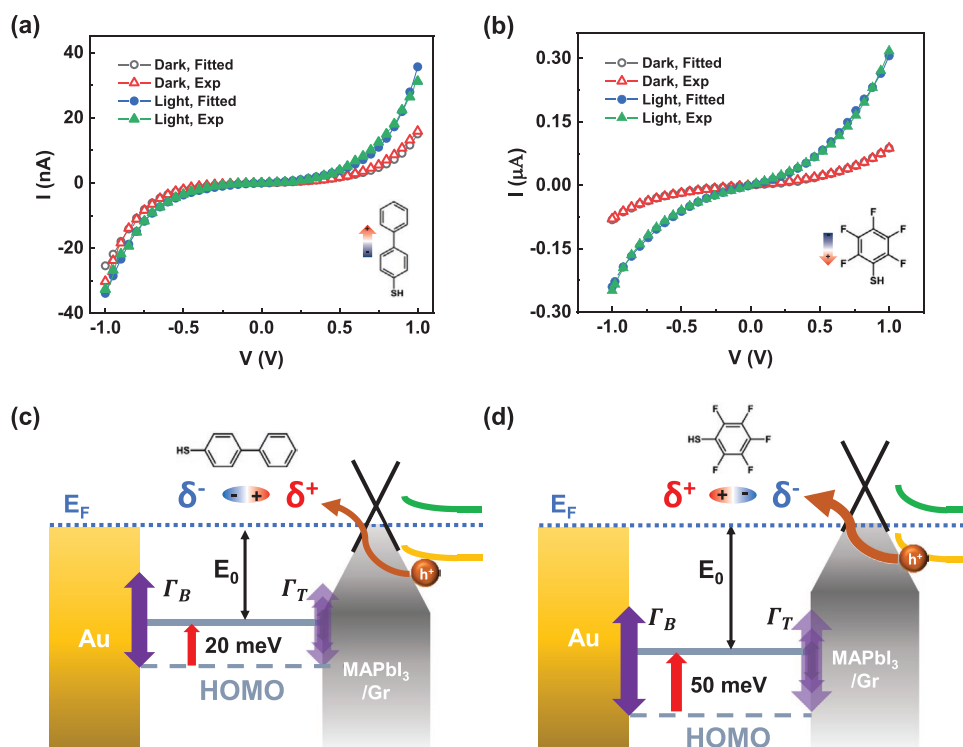


**Figure 5.** a,b) Fitting results of average  $I$ - $V$  curves for a) BPT and b) PFBT molecular junctions by using Landauer formula. Black open circles: fitted  $I$ - $V$  curves of the dark condition. Red open triangles: experimental data of the dark condition. Blue filled circles: fitted  $I$ - $V$  data of the light condition. Green filled triangles: experimental curves of the light condition. c,d) Schematic illustration of the charge transport modulation mechanism for c) BTP and d) PFBT molecular junctions.

where  $\Gamma_X$  is the electronic coupling strength between SAM and respective electrode  $X$ ,  $E_0$  is the energetic difference between the frontier orbital (HOMO level in this study) and the Fermi level of each electrode, and  $\alpha$  is the asymmetric factor. Asymmetry factor  $\alpha$ , which indicates how much the molecular orbital level is shifted when a bias is applied, takes a value of 0.5 for a symmetric junction. For example, the  $\alpha$  value was assumed to be 0.7 for the Au/ferrocene/eutectic gallium-indium (EGaIn) structure, as in several previous studies.<sup>[17,18,27,28,67,68]</sup> In our case, respective asymmetric factors were determined through the fitting process since there have been no known values for our molecular junction structures. The detailed fitting procedure is described in Section S11, Supporting Information. Briefly speaking, local minimum values of  $E_0$  and  $\Gamma_X$  were found by grid search, and converged values were obtained by gradient-descent methods. Extracted transport parameters are summarized in Table 1.

**Table 1.** Charge injection barriers ( $E_0$ ), coupling constants ( $\Gamma_X$ ), and asymmetric factors ( $\alpha$ ) extracted from the averaged  $I$ - $V$  fitting curves by employing the Landauer formula.

		$\Gamma_B$ [meV]	$\Gamma_T$ [meV]	$E_0$ [eV]	$\alpha$
BPT	Dark	44	23	0.56	0.43
	Light	44	34	0.52	0.445
BDT	Dark	49	21	0.52	0.44
	Light	49	30	0.49	0.48
PFBT	Dark	50	40	0.8	0.42
	Light	50	115	0.75	0.45

Generally, it was observed that  $E_0$  (tunneling barrier) decreased and  $\Gamma_T$  (coupling between SAM and graphene) increased for all molecules under the light condition; both cases improve the current enhancement of molecular junctions. Specifically, the  $E_0$  value decreased from 0.50 under the dark condition to 0.48 eV under the light illumination for BPT, from 0.52 to 0.49 eV for BDT, and from 0.8 to 0.75 eV for PFBT. We inferred that such light-driven barrier ( $E_0$ ) reduction occurred as photo-generated holes were transferred to graphene (see Figure 2b for the band alignment). This phenomenon results in the further p-type doping of graphene, which reduces the difference between the HOMO and the Fermi level of graphene. The  $\Gamma_B$  values, which represent the coupling strength between SAM and Au, did not change with illumination since the Au-S covalent bonding is almost unaffected by light. Since BDT and BPT make van der Waals contacts with graphene,<sup>[69]</sup> their  $\Gamma_T$  values are relatively small under the dark condition compared to those for PFBT junctions, which form F-C semi-ionic bonding with graphene (see Section S15, Supporting Information for details).<sup>[70]</sup> Under the light illumination,  $\Gamma_T$  values increased from 23 to 34 meV for BPT, from 21 to 30 meV for BDT, and from 40 to 115 meV for PFBT. Naturally,  $\Gamma_T$  values were less than  $\Gamma_B$  (44–50 meV) except the light condition of PFBT, since covalent bonds are more robust than ionic or van der Waals interactions. Asymmetric factor  $\alpha$  values also increased after the light illumination, but unlike  $E_0$  or  $\Gamma_T$ , any tendency by molecules was not observed. However, considering that  $\alpha$  values approach 0.5 (symmetric) under light conditions, it seems that the light-induced p-doping of graphene helps to



reduce asymmetry in the aspect of the band structure, further reducing the gap between  $\Gamma_B$  and  $\Gamma_T$ .

These barrier reduction and photoinduced coupling enhancement effects were the smallest in BPT and largest in PFBT, which is consistent with the observed photoinduced current enhancement as described above. The significant difference in their photoresponsivity can be accounted for by the dipole direction which is expected to modulate hole injection, and therefore inducing the  $E_0$  shift. Furthermore, given that the  $\Gamma_T$  increase was higher for PFBT than for the other molecules, we can deduce that the dipole moment is also related to the observed photoinduced coupling enhancement. Unlike BPT or BDT, the  $\delta^-$  partial charges of PFBT SAM attract numerous holes to graphene and strongly pull each other through Coulombic interaction, causing a considerable  $\Gamma_T$  increase and thereby improving the charge transport. Consequently, as depicted in Figure 5c,d, the underlying mechanism of photoinduced charge transport in MAPbI<sub>3</sub>/graphene/SAM/Au molecular junctions can be summarized to the enhanced hole injection via  $E_0$  lowering and  $\Gamma_T$  enhancement at the interface between the SAM monolayer and the top graphene/MAPbI<sub>3</sub>/electrode, both of which are assisted by the molecular dipole moments.

### 3. Conclusion

In summary, we implemented the concept of attaining photoresponsivity in molecular junctions with intrinsically low photoresponsivity by employing a photoactive electrode consisting of MAPbI<sub>3</sub>/graphene heterostructure. The photogenerated holes in MAPbI<sub>3</sub> undergo an internal-field-assisted charge transfer to graphene which triggered a significant photoinduced current enhancement in various molecular junctions. Our results clearly indicate a critical role of the SAM channel in enhancing the photocurrent generation. First, an order of magnitude photoinduced current enhancement was demonstrated by adopting different transport regimes from non-resonant to resonant tunneling according to relative frontier orbital levels of different molecules. The photocurrent could be further enhanced (maximum PDR of 1000%) by rationally selecting molecules with intrinsic dipole moments that can field-assist the charge transfer at the SAM/graphene interface. The theoretical analysis using the Landauer formalism revealed that the photoinduced energy barrier lowering and coupling effects are responsible for inducing the photocurrent in the molecular junctions. Our results demonstrate a heuristic design of photoresponsive molecular junctions via the strategic construction of the molecular active channel and heterointerfaces, in addition to the analytical framework of the charge transport that can be expanded to various molecular-based hybrid optoelectronic devices.

### 4. Experimental Section

**Synthesis of Perovskite Powder:** The authors synthesized MAPbI<sub>3</sub> single crystal powders as reported previously.<sup>[43,44]</sup> PbO powders, hydroiodic acid (HI, 57 wt% in H<sub>2</sub>O), and hydrophosphorous acid (H<sub>3</sub>PO<sub>2</sub>, 50 wt% in H<sub>2</sub>O) were purchased from Sigma-Aldrich. Methylammonium iodide (MAI) was purchased from Greatcell Solar Materials Ltd. The perovskite powder was synthesized by the inverse temperature crystallization (ITC)

method.<sup>[71]</sup> PbO (2.665 g) and MAI (1.898 g) powders were dissolved into a mixture containing 18 mL of HI and 2 mL of H<sub>3</sub>PO<sub>2</sub>. The mixed solution was heated to 120 °C on a hot plate with stirring until all the ingredients were dissolved. The solution was then cooled at room temperature. As the temperature of the solution decreased, MAPbI<sub>3</sub> powder was formed due to its decreasing solubility. After pouring the solution through Whatman filter papers, they collected and dried the synthesized MAPbI<sub>3</sub> powder in a vacuum desiccator overnight. Matching the calculated and experimental powder XRD data confirmed that a pure tetragonal phase of MAPbI<sub>3</sub> was obtained (Figure S2, Supporting Information).

**Device Fabrication:** Schematic images of the fabrication process are provided in Figure S1, Supporting Information. Since the yield of molecular devices was sensitive to the roughness of the bottom electrode, the authors used the template-stripped method to form ultra-flat surfaces.<sup>[72,73]</sup> Au bottom electrodes (50 nm thick) were deposited onto Si/SiO<sub>2</sub> substrates at the deposition rate of  $\approx 0.5 \text{ \AA s}^{-1}$  by using an electron-beam evaporator. Meanwhile, glass substrates were cleaned with acetone, isopropyl alcohol (IPA), and deionized (DI) water using a sonicator and then dried under a stream of N<sub>2</sub>. The cleaned glass substrates were further treated with reactive ion etcher using O<sub>2</sub> gas (30 sccm, 50 W, 120 s) to remove remaining organic residues. After the cleaning process, a drop of optical adhesive (OA) (Norland, no.61) was applied onto the Au-deposited Si/SiO<sub>2</sub> substrates. Then, the authors placed and pressed the cleaned glass substrates onto the applied OA to spread it evenly over each prepared Au film. All samples were exposed to ultraviolet (UV) light (1 h, 19.72 mW cm<sup>-2</sup>) to cure the OA, using a UV-ozone cleaner (AH 1700, Ahtech LTS). Afterward, they split the glass/OA/Au layers from the Si/SiO<sub>2</sub> template by inserting a razor blade into the edge of the interface between the glass/OA/Au and the Si/SiO<sub>2</sub>, carefully cleaving with gentle pressure. They made patterned device structures on these exposed surfaces by performing conventional photolithography and developing circular junctions with radii of 2  $\mu\text{m}$ . They used a diluted photoresist (PR) (AZ 5214e) by mixing propylene glycol methyl ether acetate (PGMEA) at 1:1 ratio to lower the PR wall (height of  $\approx 250 \text{ nm}$ ), so that top graphene could better contact SAM.

For the SAM formation, each sample was dipped into a 5 mm ethanol solution for 48 h in an N<sub>2</sub>-filled glove box. Afterward, the authors gently rinsed the samples with anhydrous ethanol to wash out physisorbed molecules from SAMs. For the next step, monolayer graphene was transferred as a top electrode. Monolayer graphenes were purchased from Graphene Square Inc. For this process, a poly(methyl methacrylate) (PMMA) (MicroChem Corp.) layer was spin-coated onto the monolayer graphene film as a supporting layer. To etch the Cu foil, each sample was immersed in an ammonium persulfate aqueous solution for 1 h on a 90 °C hot plate. After the etching of the Cu foil, remaining graphene films were rinsed with DI water to remove the residual etchant. Then, the floating monolayer graphene films were transferred onto the sample. The supporting polymer was removed by soaking the samples in an acetone bath, then rinsing graphene with IPA. They used the single source flash evaporation method to deposit perovskite films onto the molecular devices.<sup>[43,44]</sup> The prepared MAPbI<sub>3</sub> and MAI powders (366 mg of MAPbI<sub>3</sub> and 99.96 mg of MAI) were loaded onto a tungsten boat in a vacuum chamber. The substrates were placed with shadow masks at the height of 30 cm away from the source material. Under the vacuum condition ( $10^{-6}$  Torr), the tungsten boat was rapidly heated by applying an abrupt high current of 100 A in 3 s so that the source powder could entirely be evaporated within 30 s. In addition, since MAPbI<sub>3</sub> is easily degraded when exposed to ambient condition, they maintained every process involving MAPbI<sub>3</sub> from its deposition to electrical measurement to be conducted under vacuum condition, and samples were exposed to ambient only when transferring them from its production stage to measurement system.

**Characterization:** The electrical characteristics of the molecular devices were determined by using a semiconductor parameter analyzer (Keithley 4200 SCS) and a probe station system (JANIS Model ST-500) under vacuum condition ( $\approx 10^{-6}$  Torr). The light source was a 532 nm laser (Cobolt 04-01). Powder XRD and high-resolution XRD data

were obtained by Rigaku SmartLab. Field-emission scanning electron microscope (FE-SEM) images were collected with JSM-7800F Prime (JEOL Ltd) at an accelerating 5–10 kV voltage. Absorbance spectra were obtained using V-770 (Jasco). AFM and Kelvin probe force microscopy (KPFM) data were collected using NX-10 (Park Systems). Raman and PL spectra were measured by XperRAM 200 (Nanobase Inc.), and the time-resolved photoluminescence (TRPL) data was collected by XperRF (Nanobase Inc.). Ultraviolet photoelectron spectroscopy (UPS) spectra were collected by using AXIS SUPRA (Kratos, U.K). FIB and transmission electron microscope (TEM) data were obtained by SMI3050SE (SII Nanotechnology) and Tecnai F20 (FEI).

## Supporting Information

Supporting Information is available from the Wiley Online Library or from the author.

## Acknowledgements

C.L. and J.K. contributed equally to this work. The authors appreciate the financial support of the National Research Foundation of Korea (NRF) grant (No. 2021R1A2C3004783 and No. 2021R1C1C1010266) and the Nano-Material Technology Development Program grant (No. 2021M3H4A1A02049651) through NRF funded by the Ministry of Science and ICT (MSIT) of Korea and the industry-university cooperation program by the Samsung Electronics Co., Ltd (IO201211-08047-01). K.K. appreciates the support of the Technology Innovation Program (20013621, Center for Super Critical Material Industrial Technology) funded by the Ministry of Trade, Industry & Energy of Korea. Jeongjae L. was supported by the NRF grant funded by MSIT of Korea (No. 2019R1A6A1A10073437).

## Conflict of Interest

The authors declare no conflict of interest.

## Data Availability Statement

Research data are not shared.

## Keywords

charge transport, Landauer formalism, molecular electronics, perovskites, self-assembled monolayers

Received: January 10, 2022

Revised: March 21, 2022

Published online: April 15, 2022

- [1] J. M. Beebe, B. Kim, J. W. Gadzuk, C. D. Frisbie, J. G. Kushmerick, *Phys. Rev. Lett.* **2006**, *97*, 026801.  
 [2] H. Park, J. Park, A. K. L. Lim, E. H. Anderson, A. P. Alivisatos, P. L. McEuen, *Nature* **2000**, *407*, 57.  
 [3] M. A. Reed, C. Zhou, C. J. Muller, T. P. Burgin, J. M. Tour, *Science* **1997**, *278*, 252.  
 [4] W. Wang, T. Lee, M. A. Reed, *Phys. Rev. B* **2003**, *68*, 035416.  
 [5] B. Q. Xu, N. J. J. Tao, *Science* **2003**, *301*, 1221.

- [6] N. Xin, J. Guan, C. Zhou, X. Chen, C. Gu, Y. Li, M. A. Ratner, A. Nitzan, J. F. Stoddart, X. Guo, *Nat. Rev. Phys.* **2019**, *1*, 211.  
 [7] C. Jia, A. Migliore, N. Xin, S. Huang, J. Wang, Q. Yang, S. Wang, H. Chen, D. Wang, B. Feng, Z. Liu, G. Zhang, D.-H. Qu, H. Tian, M. A. Ratner, H. Q. Xu, A. Nitzan, X. Guo, *Science* **2016**, *352*, 1443.  
 [8] D. Xiang, X. Wang, C. Jia, T. Lee, X. Guo, *Chem. Rev.* **2016**, *116*, 4318.  
 [9] H. Fu, X. Zhu, P. Li, M. Li, L. Yang, C. Jia, X. Guo, *J. Mater. Chem. C* **2022**, *10*, 2375.  
 [10] F. Schwarz, G. Kastlunger, F. Lissel, C. Egler-Lucas, S. N. Semenov, K. Venkatesan, H. Berke, R. Stadler, E. Lortscher, *Nat. Nanotechnol.* **2016**, *11*, 170.  
 [11] L. J. Cui, R. J. Miao, K. Wang, D. Thompson, L. A. Zotti, J. C. Cuevas, E. Meyhofer, P. Reddy, *Nat. Nanotechnol.* **2018**, *13*, 122.  
 [12] H. Song, Y. Kim, Y. H. Jang, H. Jeong, M. A. Reed, T. Lee, *Nature* **2009**, *462*, 1039.  
 [13] M. Paulsson, S. Datta, *Phys. Rev. B* **2003**, *67*, 241403.  
 [14] P. Reddy, S.-Y. Jang, R. A. Segalman, A. Majumdar, *Science* **2007**, *315*, 1568.  
 [15] S. Park, H. J. Yoon, *Nano Lett.* **2018**, *18*, 7715.  
 [16] S. Park, J. Jang, H. Kim, D. I. Park, K. Kim, H. J. Yoon, *J. Mater. Chem. A* **2020**, *8*, 19746.  
 [17] C. A. Nijhuis, W. F. Reus, G. M. Whitesides, *J. Am. Chem. Soc.* **2010**, *132*, 18386.  
 [18] C. A. Nijhuis, W. F. Reus, J. R. Barber, M. D. Dickey, G. M. Whitesides, *Nano Lett.* **2010**, *10*, 3611.  
 [19] V. B. Engelkes, J. M. Beebe, C. D. Frisbie, *J. Am. Chem. Soc.* **2004**, *126*, 14287.  
 [20] B. Kim, S. H. Choi, X. Y. Zhu, C. D. Frisbie, *J. Am. Chem. Soc.* **2011**, *133*, 19864.  
 [21] X. P. Chen, M. Roemer, L. Yuan, W. Du, D. Thompson, E. del Barco, C. A. Nijhuis, *Nat. Nanotechnol.* **2017**, *12*, 797.  
 [22] G. D. Kong, J. Jin, M. Thuo, H. Song, J. F. Joung, S. Park, H. J. Yoon, *J. Am. Chem. Soc.* **2018**, *140*, 12303.  
 [23] G. D. Kong, M. Kim, H.-J. Jang, K.-C. Liao, H. J. Yoon, *Phys. Chem. Chem. Phys.* **2015**, *17*, 13804.  
 [24] J. C. Love, L. A. Estroff, J. K. Kriebel, R. G. Nuzzo, G. M. Whitesides, *Chem. Rev.* **2005**, *105*, 1103.  
 [25] H. B. Akkerman, P. W. M. Blom, D. M. de Leeuw, B. de Boer, *Nature* **2006**, *441*, 69.  
 [26] R. C. Chiechi, E. A. Weiss, M. D. Dickey, G. M. Whitesides, *Angew. Chem., Int. Ed.* **2008**, *47*, 142.  
 [27] G. Wang, Y. Kim, S. I. Na, Y. H. Kahng, J. Ku, S. Park, Y. H. Jang, D. Y. Kim, T. Lee, *J. Phys. Chem. C* **2011**, *115*, 17979.  
 [28] Y. Jang, S. J. Kwon, J. Shin, H. Jeong, W. T. Hwang, J. Kim, J. Koo, T. Y. Ko, S. Ryu, G. Wang, T. W. Lee, T. Lee, *ACS Appl. Mater. Interfaces* **2017**, *9*, 42043.  
 [29] M. Min, S. Seo, S. M. Lee, H. Lee, *Adv. Mater.* **2013**, *25*, 7045.  
 [30] D. Kos, D. R. Assumpcao, C. Y. Guo, J. J. Baumberg, *ACS Nano* **2021**, *15*, 14535.  
 [31] A. M. Najarian, R. L. McCreery, *ACS Nano* **2019**, *13*, 867.  
 [32] T. Sendler, K. Luka-Guth, M. Wieser, Lokamani, J. W. , M. Helm, S. Gemming, J. Kerbusch, E. Scheer, T. Huhn, A. Erbe, *Adv. Sci.* **2015**, *2*, 1500017.  
 [33] D. Kim, H. Jeong, W. T. Hwang, Y. Jang, D. Sysoiev, E. Scheer, T. Huhn, M. Min, H. Lee, T. Lee, *Adv. Funct. Mater.* **2015**, *25*, 5918.  
 [34] J. Koo, Y. Jang, L. Martin, D. Kim, H. Jeong, K. Kang, W. Lee, J. Kim, W. T. Hwang, D. Xiang, E. Scheer, M. Kabdulov, T. Huhn, F. Pauly, T. Lee, *ACS Appl. Mater. Interfaces* **2019**, *11*, 11645.  
 [35] S. Seo, M. Min, S. M. Lee, H. Lee, *Nat. Commun.* **2013**, *4*, 1920.  
 [36] M. A. Green, A. Ho-Baillie, H. J. Snaith, *Nat. Photonics* **2014**, *8*, 506.  
 [37] B. R. Sutherland, E. H. Sargent, *Nat. Photonics* **2016**, *10*, 295.  
 [38] H. J. Snaith, *Nat. Mater.* **2018**, *17*, 372.  
 [39] J. Kim, W. Lee, K. Cho, H. Ahn, J. Lee, K.-Y. Baek, J.-K. Kim, K. Kang, T. Lee, *Nanotechnology* **2021**, *32*, 185203.

- [40] M. A. Haque, M. I. Nugraha, S. H. K. Paleti, D. Baran, *J. Phys. Chem. C* **2019**, *123*, 14928.
- [41] A. H. Castro Neto, F. Guinea, N. M. R. Peres, K. S. Novoselov, A. K. Geim, *Rev. Mod. Phys.* **2009**, *81*, 109.
- [42] S. J. Kim, J. Ryu, S. Son, J. M. Yoo, J. B. Park, D. Won, E. K. Lee, S. P. Cho, S. Bae, S. Cho, B. H. Hong, *Chem. Mater.* **2014**, *26*, 2332.
- [43] W. Lee, J. Lee, H. D. Lee, J. Kim, H. Ahn, Y. Kim, D. Yoo, J. Lee, T. W. Lee, K. Kang, T. Lee, *Sci. Rep.* **2020**, *10*, 18781.
- [44] J. Lee, W. Lee, J. Lee, K. Y. Baek, J. Shin, J. K. Kim, J. Kim, H. Ahn, K. Kang, T. Lee, *Adv. Mater. Technol.* **2021**, *6*, 2001131.
- [45] J. M. Tour, L. Jones, D. L. Pearson, J. J. S. Lamba, T. P. Burgin, G. M. Whitesides, D. L. Allara, A. N. Parikh, S. Atre, *J. Am. Chem. Soc.* **1995**, *117*, 9529.
- [46] Y. Kim, T. Pietsch, A. Erbe, W. Belzig, E. Scheer, *Nano Lett.* **2011**, *11*, 3734.
- [47] E. Scheer, J. C. Cuevas, *Molecular Electronics: An Introduction to Theory and Experiment*, World Scientific, 2nd ed., Singapore **2017**.
- [48] Y. Lee, J. Kwon, E. Hwang, C.-H. Ra, W. J. Yoo, J.-H. Ahn, J. H. Park, J. H. Cho, *Adv. Mater.* **2015**, *27*, 41.
- [49] Y. Wang, Y. Zhang, Y. Lu, W. Xu, H. Mu, C. Chen, H. Qiao, J. Song, S. Li, B. Sun, Y.-B. Cheng, Q. Bao, *Adv. Opt. Mater.* **2015**, *3*, 1389.
- [50] P.-H. Chang, S.-Y. Liu, Y.-B. Lan, Y.-C. Tsai, X.-Q. You, C.-S. Li, K.-Y. Huang, A.-S. Chou, T.-C. Cheng, J.-K. Wang, C.-I. Wu, *Sci. Rep.* **2017**, *7*, 46281.
- [51] O. Malinkiewicz, A. Yella, Y. H. Lee, G. M. Espallargas, M. Graetzel, M. K. Nazeeruddin, H. J. Bolink, *Nat. Photonics* **2014**, *8*, 128.
- [52] M. Caputo, N. Cefarin, A. Radivo, N. Demitri, L. Gigli, J. R. Plaisier, M. Panighel, G. Di Santo, S. Moretti, A. Giglia, M. Polentarutti, F. De Angelis, E. Mosconi, P. Umari, M. Tormen, A. Goldoni, *Sci. Rep.* **2019**, *9*, 15159.
- [53] P. Schulz, E. Edri, S. Kirmayer, G. Hodes, D. Cahen, A. Kahn, *Energy Environ. Sci.* **2014**, *7*, 1377.
- [54] Z. Zhu, J. Ma, Z. Wang, C. Mu, Z. Fan, L. Du, Y. Bai, L. Fan, H. Yan, D. L. Phillips, S. Yang, *J. Am. Chem. Soc.* **2014**, *136*, 3760.
- [55] R. S. Yan, Q. Zhang, W. Li, I. Calizo, T. Shen, C. A. Richter, A. R. H. Walker, X. L. Liang, A. Seabaugh, D. Jena, H. G. Xing, D. J. Gundlach, N. V. Nguyen, *Appl. Phys. Lett.* **2012**, *101*, 022105.
- [56] R. M. Feenstra, D. Jena, G. Gu, *J. Appl. Phys.* **2012**, *111*, 043711.
- [57] Y. Yin, Z. G. Cheng, L. Wang, K. J. Jin, W. Z. Wang, *Sci. Rep.* **2014**, *4*, 5758.
- [58] S. S. Pingale, *Phys. Chem. Chem. Phys.* **2011**, *13*, 15158.
- [59] H. J. Yoon, N. D. Shapiro, K. M. Park, M. M. Thuo, S. Soh, G. M. Whitesides, *Angew. Chem., Int. Ed.* **2012**, *51*, 4658.
- [60] H. J. Yoon, C. M. Bowers, M. o. Baghbanzadeh, G. M. Whitesides, *J. Am. Chem. Soc.* **2014**, *136*, 16.
- [61] M. Baghbanzadeh, L. Belding, L. Yuan, J. Park, M. H. Al-Sayah, C. M. Bowers, G. M. Whitesides, *J. Am. Chem. Soc.* **2019**, *141*, 8969.
- [62] J. S. Eo, J. Shin, S. Yang, T. Jeon, J. Lee, S. Choi, C.-H. Lee, G. Wang, *Adv. Sci.* **2021**, *8*, 2101390.
- [63] H. Kang, S. Seong, E. Ito, T. Isoshima, M. Hara, H. J. Yoon, J. Noh, *Appl. Surf. Sci.* **2021**, *555*, 149671.
- [64] J. G. Simmons, *J. Appl. Phys.* **1963**, *34*, 1793.
- [65] X. Guo, *Molecular-Scale Electronics: Current Status and Perspectives*, Springer, Cham, Switzerland **2018**, pp. 377.
- [66] S. Datta, *Quantum Transport: Atom to Transistor*, Cambridge University Press, New York **2005**, pp. 404.
- [67] N. Nerngchamnong, L. Yuan, D.-C. Qi, J. Li, D. Thompson, C. A. Nijhuis, *Nat. Nanotechnol.* **2013**, *8*, 113.
- [68] C. A. Nijhuis, W. F. Reus, G. M. Whitesides, *J. Am. Chem. Soc.* **2009**, *131*, 17814.
- [69] Y. Jang, H. Jeong, D. Kim, W.-T. Hwang, I. Jeong, H. Song, H. Jeong, M. Min, T. Lee, *J. Nanosci. Nanotechnol.* **2016**, *16*, 8565.
- [70] J. Kim, R. Zhou, K. Murakoshi, S. Yasuda, *RSC Adv.* **2018**, *8*, 14152.
- [71] M. I. Saidaminov, A. L. Abdelhady, B. Murali, E. Alarousu, V. M. Burlakov, W. Peng, I. Dursun, L. Wang, Y. He, G. Maculan, A. Goriely, T. Wu, O. F. Mohammed, O. M. Bakr, *Nat. Commun.* **2015**, *6*, 7586.
- [72] L. Yuan, L. Jiang, D. Thompson, C. A. Nijhuis, *J. Am. Chem. Soc.* **2014**, *136*, 6554.
- [73] S. K. Karuppannan, H. Hongting, C. Troadec, A. Vilan, C. A. Nijhuis, *Adv. Funct. Mater.* **2019**, *29*, 1904452.